Perovskite Oxide Absorbents for Oxygen Separation

Yufeng He
State Key Laboratory of Catalysis, Dalian Institute of Chemical Physics, Chinese Academy of Sciences, Dalian 116023, China

Graduate School of the Chinese Academy of Sciences, Beijing 100049, China

Xuefeng Zhu
State Key Laboratory of Catalysis, Dalian Institute of Chemical Physics, Chinese Academy of Sciences, Dalian 116023, China

Qiming Li
State Key Laboratory of Catalysis, Dalian Institute of Chemical Physics, Chinese Academy of Sciences, Dalian 116023, China

Graduate School of the Chinese Academy of Sciences, Beijing 100049, China

Weishen Yang
State Key Laboratory of Catalysis, Dalian Institute of Chemical Physics, Chinese Academy of Sciences, Dalian 116023, China

DOI 10.1002/aic.11931
Published online July 30, 2009 in Wiley InterScience (www.interscience.wiley.com).

The fixed-bed oxygen absorption processes of the series of $Ba_{1-x}Sr_xCo_{0.8}Fe_{0.2}O_{3-\delta}$ oxides were studied by oxygen partial pressure swing absorption in the temperature range of 300–850°C. The results show that $SrCo_{0.8}Fe_{0.2}O_{3-\delta}$, with the smallest A-site ion radius, has the largest oxygen absorption capacity (0.402 mmol/g) at 500°C. The oxygen absorption and desorption kinetics fit well with the pseudo-second-order kinetics model. Comparing the modeling absorption rate coefficient k_2 with the desorption rate coefficient k_2', all the oxides studied had higher oxygen absorption rates than oxygen desorption ones. In addition, the combined results of X-ray diffraction analysis, O_2-TPD, room temperature iodometric titration, and thermogravimetric analysis explained the relationship between the oxygen absorption capacities and the average radii of the A-site ions for this series of $Ba_{1-x}Sr_xCo_{0.8}Fe_{0.2}O_{3-\delta}$ in the temperature range of 300–600°C. © 2009 American Institute of Chemical Engineers *AIChE J,* 55: 3125–3133, 2009
Keywords: $Ba_{1-x}Sr_xCo_{0.8}Fe_{0.2}O_{3-\delta}$, perovskite oxides, oxygen absorption/desorption, ionic radius

Introduction

The production of oxygen by air separation is an important chemical engineering process. Nowadays, there are three main air separation processes: cryogenic distillation, pressure swing adsorption (PSA), and membrane separation.[1]

Correspondence concerning this article should be addressed to W. S. Yang at yangws@dicp.ac.cn

Cryogenic distillation technology, which requires a large-scale plant and high investment, is widely used for producing high-purity oxygen (oxygen concentration $\geq$ 99%). Zeolites (A, X, and Y) absorbents, with their advantages of low investment, low energy consumption and easy handling, have already been used in commercial pressure swing adsorption (PSA). Polymer membranes with their merits of low cost and easy fabrication or molding, need to be operated under rigorous conditions, including not too high temperature and pressure and not corrosive environments. The oxygen produced by polymer membranes is oxygen-enriched air (oxygen concentration about 40–50%). However, the amount of nitrogen in air is nearly four times that of oxygen, and zeolites usually adsorb nitrogen not oxygen, so it means that larger quantities of absorbents are needed for air separation.[2] Thus, new and more efficient absorbent materials are needed to meet industrial demands. As reported by Lin's group,[3,4] perovskite-type absorbent materials with variable oxygen content have some important characteristics which might overcome the drawbacks of zeolite absorbents. These characteristics include an infinite selectivity of O_2 over N_2 or other gases, a high oxygen absorption rate and a large oxygen absorption capacity. Karppinen et al.[5] and Hu's group[6–9] investigated the oxygen absorption/desorption properties of $YBaCo_4O_{7+\delta}$ and $YBa_2Cu_3O_{7-\delta}$, $REBaCo_2O_{5+\delta}$ (RE = Pr, Gd, Y), and their dopant oxides by a TG technique. Guntuka et al. also engaged in this field, and they investigated the oxygen absorption/desorption characteristics of A- and B-site substituted lanthanum cobaltite perovskite oxides.[10,11]

Perovskite oxides (ABO_3), where the replacement of A or B or both results in drastic changes of properties, have been widely studied as catalysts for hydrocarbon oxidation, as cathode materials for SOFCs, and as oxygen separation membranes for air separation or integrated with methane partial oxidation. When the B-site ions take a mixed-valence state, partial or total substitution of the A-site cations by other metal ions with lower valences generally leads to the formation of oxygen vacancies and/or a change of the average oxidation states of the B-site ions to maintain the charge neutrality.[12] Teraoka et al. initially investigated the absorption/desorption properties of Sr-substituted lanthanum cobalt (iron) oxides $La_{1-x}Sr_xCo_{1-y}Fe_yO_{3-\delta}$.[13–15] TPD experiments indicated that the amount of oxygen desorbed at low temperature increased with the substitution of La^{3+} by Sr^{2+}. It was shown that the partial or total substitution of La^{3+} by Sr^{2+} increased the average oxidation state of the B-site ions from Co^{3+} (Fe^{3+}) to Co^{4+} (Fe^{4+}), as well as producing oxygen vacancies. As early as 1979, it was reported that on cooling in a flow of oxygen or heating in a vacuum, the perovskite oxide $La_{1-x}Sr_xCoO_{3-\delta}$ absorbed or desorbed a large amount of oxygen, and the amount increased with the Sr content of the oxide.[13] The properties of the composite oxides $La_{1-x}A_xCo_{1-y}Fe_yO_{3-\delta}$ (A = Ba, Sr, Ca) have been widely studied as oxygen permeation membranes by many groups.[16–23] Therefore, it is suggested that if these $La_{1-x}A_xCo_{1-y}Fe_yO_{3-\delta}$ (A = Ba, Sr, Ca) perovskite oxides can be used as oxygen absorbents, it might lead to an unforeseen change in chemical industry. As mentioned above, when the trivalent La is completely substituted by the divalent alkali earth ions A (A = Ba, Sr, Ca), this will create the greatest number of oxygen vacancies and/or B^{4+} (Co^{4+}, Fe^{4+}) in the $La_{1-x}A_xCo_{1-y}Fe_yO_{3-\delta}$ oxides, and might result in the highest oxygen absorption or desorption capacities. The oxygen desorption properties of the series of $Ba_{1-x}Sr_xCo_{0.8}Fe_{0.2}O_{3-\delta}$ have been systematically investigated using the O_2-TPD technique in our laboratory.[24] The results revealed that A-site ions had considerable influence on the oxygen desorption capacities.

Although complex oxides, especially perovskite materials which theoretically have an infinite selectivity for oxygen, have received significant attention as oxygen permeation membranes for air separation, the membrane technology is still far away from being industrially applicable due to the poor stability of their chemical and mechanical properties, and the difficulties of fabrication and sealing.[25,26] If perovskite oxides are used as oxygen absorbents for air separation on a fixed-bed apparatus, they go through almost the same processes as membrane permeation, including two surface oxygen exchanges and one O^{2-} diffusion process. In this way, the oxygen separation process may overcome the problems appearing in the permeation membrane technology, and high purity oxygen can be produced via evacuation.

In this article, $Ba_{1-x}Sr_xCo_{0.8}Fe_{0.2}O_{3-\delta}$ oxides were selected to investigate the influences of the A-site ions on the oxygen absorption/desorption properties within the temperature range of 300–850°C. These materials were systematically studied by stable state oxygen absorption processes. X-ray diffraction analysis, oxygen temperature-programmed desorption (O_2-TPD), room temperature iodometric titration, and thermogravimetric analysis (TGA) were also applied to investigate the properties of these oxides.

Experimental

Preparation of materials

Powders of the $Ba_{1-x}Sr_xCo_{0.8}Fe_{0.2}O_{3-\delta}$ oxides were synthesized by a combined EDTA-citric acid complexing method, as described in reference.[27] Concentrations of metal nitrates solution were determined by titration. In the synthesis process, the calculated amount of $Ba(NO_3)_2$ ($\geq$99.5%) was dissolved in EDTA-$NH_3.H_2O$ with heating and stirring, then the appropriate proportions of $Sr(NO_3)_2$ ($\geq$99.5%), $Co(NO_3)_2{\cdot}6H_2O$ ($\geq$99.0%), $Fe(NO_3)_3{\cdot}9H_2O$ ($\geq$98.5%) were added to the solution. After stirring for about half an hour, appropriate amount of citric acid was introduced. Finally, the mole ratio of EDTA, citric acid and total metal ions is 1:1:1. NH_3 H_2O was added to adjust the solution pH value to around 6, at which point the solution became transparent. During the whole heating and stirring process, the pH value of the solution was maintained at around 6, because EDTA-NH_3 H_2O and citric acid formed a buffering solution. With heating and stirring using a magnetic stirrer, the polymerization and condensation reactions took place, and a dark purple gel was obtained. Then the as-prepared gel was heated on an electric stove till self-ignition took place, and a primary powder with the desired stoichiometry was obtained. The green powder was calcined in air at 950°C for 5 h. The resultant powders were tested by XRD, SEM, TGA, and iodometric titration. Absorbent granules, for stable state oxygen absorption and O_2-TPD experiments, were prepared by pressing powders into pellets in a stainless steel mold

(34 mm in diameter) under a hydraulic pressure of 75 MPa, followed by crushing and sieving to 20–40 mesh.

Characterization of materials

The crystal structures of the synthesized sample powders were checked by X-ray diffraction (XRD, Rigaku D/Max-RB, Cu Kα radiation) in the 2θ range of 20–80° with a step width of 0.02°. The particle sizes of the resulting samples were observed on a scanning electron microscopy (SEM; Quanta 200 FEG, FEI Company, operating at 20 kV).

Oxygen desorption properties of these oxides were investigated by the O_2-TPD technique. 1.0 g of each sample was packed into a quartz tube. Helium was used as the carrier gas with a flow rate of 40 ml/min. The temperature was increased from 100°C to 1000°C at a rate of 10°C/min. A thermal conductivity detector (TCD) was equipped on line for signal detection, along with a computer data acquisition system.

Oxygen nonstoichiometries and the average oxidation states of the B-site ions at room temperature were determined by an iodometric titration.[28–30] The principle of the iodometric titration is that the B-site transition metal ions with higher oxidation state (B^{3+} and/or B^{4+}) can oxidize iodide ions (I^-) to iodine (I_2). Thus by means of the amount of iodide ions oxidized to iodine and the equations of their reactions, the oxygen nonstoichiometry and the average oxidation state of the B-site cations of a perovskite-type oxide could be calculated.

TGA was performed on a thermogravimetric/differential thermal analyzer (Pyris Diamond TG/DTA). Measurements were carried out at 530°C in two kinds of gas atmospheres. Synthesized air (O_2, 21%) was used for the oxygen absorption processes, with high purity nitrogen for oxygen desorption or the so-called absorbent regeneration processes. The flow rates of air and nitrogen were both 100 ml/min. Samples of powders for the tests weighed about 50 mg.

Oxygen absorption/desorption of materials

The oxygen absorption experiments were performed on a fixed-bed oxygen absorption apparatus, as shown in Figure 1. Figure 1a is a schematic diagram of the oxygen absorption measurement setup, consisting of a gas delivery system, a temperature controlling system, an oxygen absorption column, an oxygen sensor (GPR-3100, Advanced Instruments), and a computer for data storage. A quartz tube acted as the oxygen absorption column, and its dimensions are shown in Figure 1b. Two calibrated thermocouples were used to monitor the temperatures of the furnace and the absorption bed. One was inserted into the absorption column in contact with absorbent grains to display the thermal effects of the oxygen absorption (desorption) process; the other was placed in the interspace between the quartz tube and the furnace to monitor the temperature of the furnace. Exothermic (endothermic) heat could be estimated by the different temperatures between the two thermocouples. During measurements, the oxygen concentrations in the effluent gases exiting from the absorption column were continuously monitored by the oxygen sensor. Data collection and storage were performed by the computer.

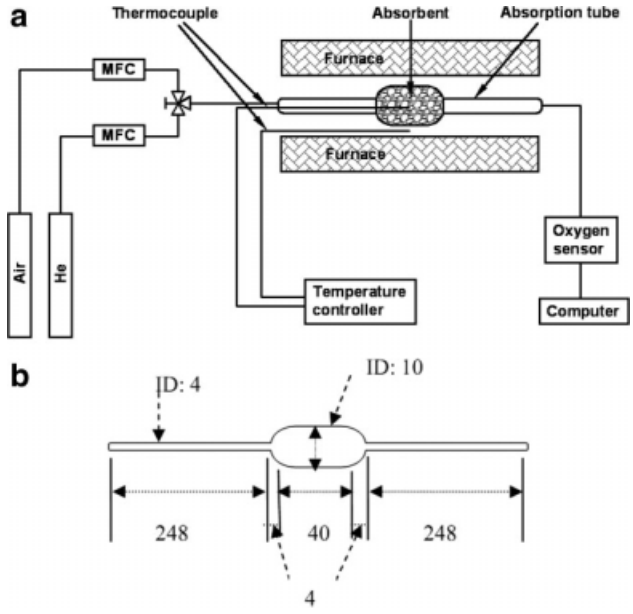

Figure 1. (a) Schematic diagram of the oxygen absorption setup; (b) dimensions of the oxygen absorption tube (units: mm).

MFC: Mass flow meter; ID: inside diameter.

The operation temperatures for all samples were in the range of 300–850°C, and the gas pressures were both 1 atm. Synthesized air and high purity helium (P_{O2}, 10^{-5} atm) were used for oxygen absorptions and absorbent regenerations, respectively. During all the oxygen absorption/desorption experiments, the air and helium fluxes were kept at about 50 and 100 ml/min, respectively. The oxygen absorption/desorption capacities in this article were all corrected for dead-volume times.

Results and Discussion

The room temperature X-ray diffraction patterns, shown in Figure 2, indicate that among the series of $Ba_{1-x}Sr_xCo_{0.8}Fe_{0.2}O_{3-\delta}$ oxides, the samples with Sr content $x > 0.3$ are single-phase cubic perovskites, while those with $x < 0.3$ exhibit different diffraction crystal patterns from that of cubic perovskite structure. These results, together with the XRD results reported by Shao et al.,[24] suggest that $Ba_{0.7}Sr_{0.3}Co_{0.8}Fe_{0.2}O_{3-\delta}$ ($x = 0.3$) is a transition material between the pure cubic perovskites and noncubic perovskite oxides among the series of $Ba_{1-x}Sr_xCo_{0.8}Fe_{0.2}O_{3-\delta}$.

Oxygen partial pressure swing absorption experiments were performed to test the oxygen absorption and desorption properties of $Ba_{1-x}Sr_xCo_{0.8}Fe_{0.2}O_{3-\delta}$. At each temperature, the equilibrium oxygen absorption/desorption processes were carried out, and the results of the oxygen absorption capacities are shown in Figure 3. The oxygen absorption/desorption capacities are calculated by the following equations:

$$\text{Absorption process}: q_{abs} = \frac{1}{m}\int_0^t (F_{air}x_{in} - F_{out}x_{out})dt \quad (1)$$

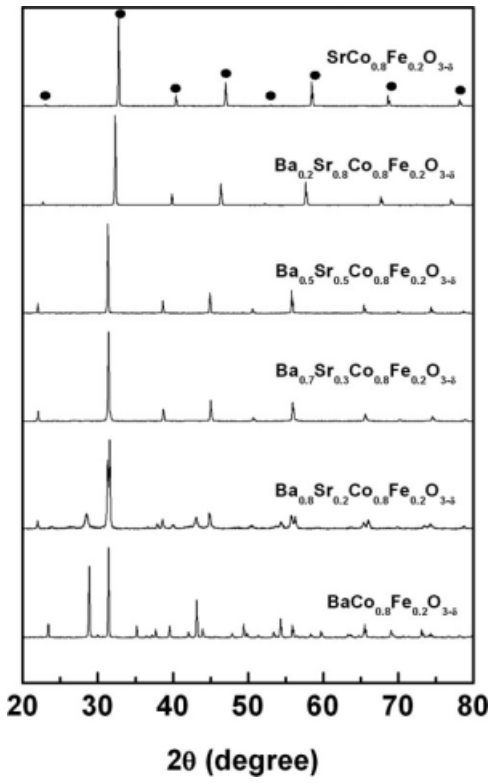

Figure 2. Room temperature X-ray diffraction patterns for the series of $Ba_{1-x}Sr_xCo_{0.8}Fe_{0.2}O_{3-\delta}$ oxides.

● Peak of cubic perovskite.

$$\text{Desorption process}: q_{\text{des}} = \frac{1}{m}\int_0^t (F_{\text{out}}x_{\text{out}})dt \qquad (2)$$

For the above two equations, the expressions for F_{out} are:

$$\text{Absorption process}: F_{\text{out}} = F_{\text{air}}\left(\frac{1-x_{\text{in}}}{1-x_{\text{out}}}\right) \qquad (3)$$

$$\text{Desorption process}: F_{\text{out}} = \frac{F_{\text{He}}}{1-x_{\text{out}}} \qquad (4)$$

Substituting Eq. 3 into Eqs. 1 and 4 into (2)[31] gives:

$$\text{Absorption process}: q_{\text{abs}} = \frac{F_{\text{air}}}{m}\int_0^t \left(\frac{x_{\text{in}}-x_{\text{out}}}{1-x_{\text{out}}}\right)dt \qquad (5)$$

$$\text{Desorption process}: q_{\text{des}} = \frac{F_{\text{He}}}{m}\int_0^t \left(\frac{x_{\text{out}}}{1-x_{\text{out}}}\right)dt \qquad (6)$$

where q_{abs} (q_{des}) is the oxygen absorption (desorption) capacity, F_{air} (F_{He}) and F_{out} are the fluxes of the synthesized air (pure helium) and that exiting from the absorption column during the oxygen absorption/desorption process, t and m are the oxygen absorption/desorption time and the weight of an oxide sample, x_{in} and x_{out} are the oxygen mole fractions in the feed air and F_{out}, respectively. Figure 4 compares the oxygen absorption/desorption processes at 500°C. It is evident from

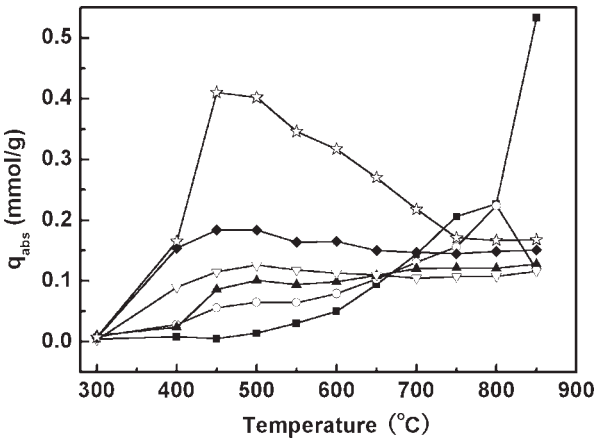

Figure 3. Oxygen absorption capacities of the $Ba_{1-x}Sr_xCo_{0.8}Fe_{0.2}O_{3-\delta}$ series in the temperature range of 300–850°C.

—■—$BaCo_{0.8}Fe_{0.2}O_{3-\delta}$, —○—$Ba_{0.8}Sr_{0.2}Co_{0.8}Fe_{0.2}O_{3-\delta}$, —▲—$Ba_{0.7}Sr_{0.3}Co_{0.8}Fe_{3-\delta}$, —▽—$Ba_{0.5}Sr_{0.5}Co_{0.8}Fe_{0.2}O_{3-\delta}$, —◆—$Ba_{0.2}Sr_{0.8}Co_{0.8}Fe_{0.2}O_{3-\delta}$, —☆—$SrCo_{0.8}Fe_{0.2}O_{3-\delta}$.

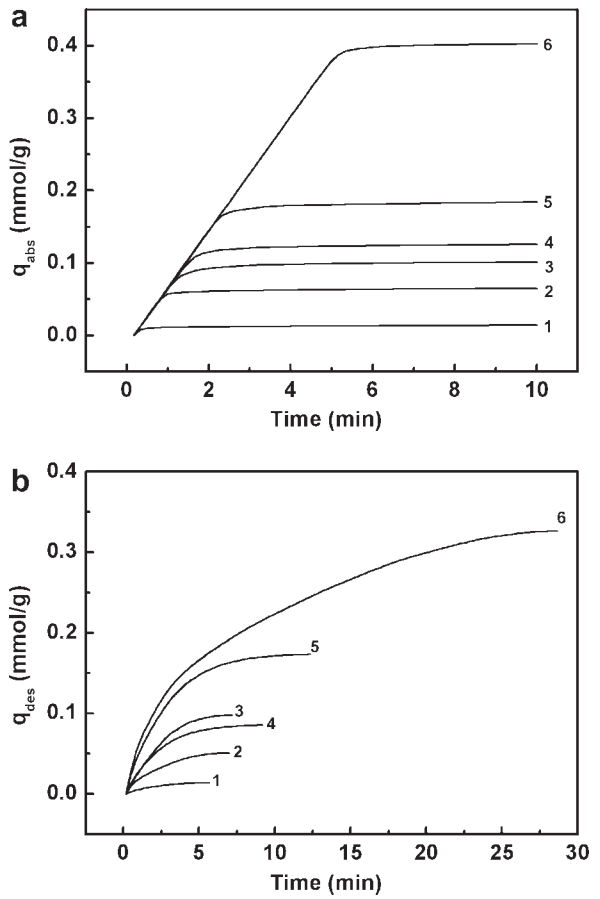

Figure 4. (a) Oxygen absorption kinetics curves and (b) oxygen desorption kinetics curves for the samples at 500°C.

1. $BaCo_{0.8}Fe_{0.2}O_{3-\delta}$, 2. $Ba_{0.8}Sr_{0.2}Co_{0.8}Fe_{0.2}O_{3-\delta}$, 3. $Ba_{0.7}Sr_{0.3}Co_{0.8}Fe_{0.2}O_{3-\delta}$, 4. $Ba_{0.5}Sr_{0.5}Co_{0.8}Fe_{0.2}O_{3-\delta}$, 5. $Ba_{0.2}Sr_{0.8}Co_{0.8}Fe_{0.2}O_{3-\delta}$, 6. $SrCo_{0.8}Fe_{0.2}O_{3-\delta}$.

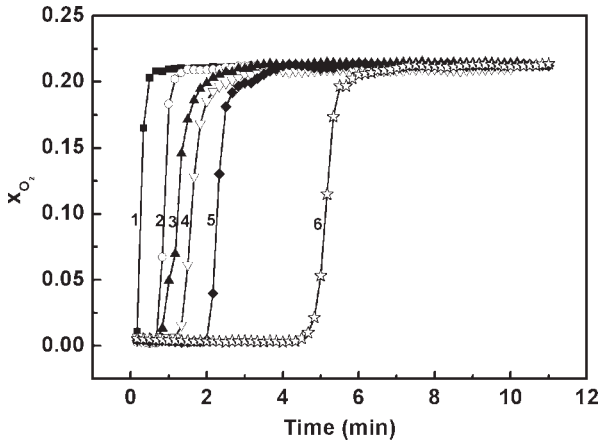

Figure 5. Mole fractions of oxygen in the effluent exiting from the absorption tube during the oxygen absorption processes.

x_{O2}: Mole fraction of oxygen in effluent air —■— $BaCo_{0.8}Fe_{0.2}O_{3-\delta}$, —○— $Ba_{0.8}Sr_{0.2}Co_{0.8}Fe_{0.2}O_{3-\delta}$, —▲— $Ba_{0.7}Sr_{0.3}Co_{0.8}Fe_{3-\delta}$, —▽— $Ba_{0.5}Sr_{0.5}Co_{0.8}Fe_{0.2}O_{3-\delta}$, —◆— $Ba_{0.2}Sr_{0.8}Co_{0.8}Fe_{0.2}O_{3-\delta}$, —☆— $SrCo_{0.8}Fe_{0.2}O_{3-\delta}$,

Figures 3 and 4 that at low temperature the oxygen absorption capacities of these samples increase with Sr contents (decrease with the increase of average radii of A-site ions). Figure 3 also indicates that the single-phase cubic perovskite oxides $Ba_{1-x}Sr_xCo_{0.8}Fe_{0.2}O_{3-\delta}$ ($x > 0.3$) prefer to absorb oxygen at lower temperature, while $Ba_{1-x}Sr_xCo_{0.8}Fe_{0.2}O_{3-\delta}$ ($x = 0$, 0.2, 0.3) have the characteristics of oxygen absorption at higher temperature. Therefore, the material $SrCo_{0.8}Fe_{0.2}O_{3-\delta}$ with the smallest A-site ionic radius absorbs the largest amount of oxygen at low temperature ($T = 500$°C). The previous studies of the O_2-TPD of $Ba_{1-x}Sr_xCo_{0.8}Fe_{0.2}O_{3-\delta}$ in our group revealed the phenomenon that most perovskite oxides exhibit two kinds of oxygen desorption peaks (α-/β-oxygen),[24] which were related to the lower and higher temperature oxygen absorption peaks in Figure 3, respectively. As revealed in Figure 4a, each plot comprises two sections. The first part is linear, and the second is curved, gradually tending to form a plateau (the equilibrium oxygen absorption capacity). Figure 5 shows the mole fractions of oxygen in the effluent air exiting from the absorption tube during the oxygen absorption processes. The linear parts (in Figure 4a) correspond to the low plane sections (x_{out} close to zero) before the breakthrough curves (in Figure 5), while the others (in Figure 4a) correspond to the steep uptake parts of the breakthrough curves (in Figure 5) up to the higher oxygen mole fraction plateaus, ending with the mole fraction of oxygen in air $x_{out} \approx 0.21$. Therefore, for the linear sections in Figure 4a ($x_{out} \approx 0$), the oxygen absorption processes can be expressed:

$$q_{abs(1)} = \frac{F_{air}}{m} \int_0^t x_{in} \cdot dt = \frac{F_{air}}{m} \cdot x_{in} \cdot t \tag{7}$$

Therefore, with the same ratio of the inlet air fluxes F_{air} to the corresponding absorbent weights m, the transient rates for the low planar parts in Figure 5 are the same, and the linear parts in Figure 4a have the same slope when the absorbents are subjected to sudden changes from helium to air:

$$q_{abs(1)} = k_o \cdot t \tag{8}$$

$$k_o = \frac{F_{air}}{m} \cdot x_{in} \tag{9}$$

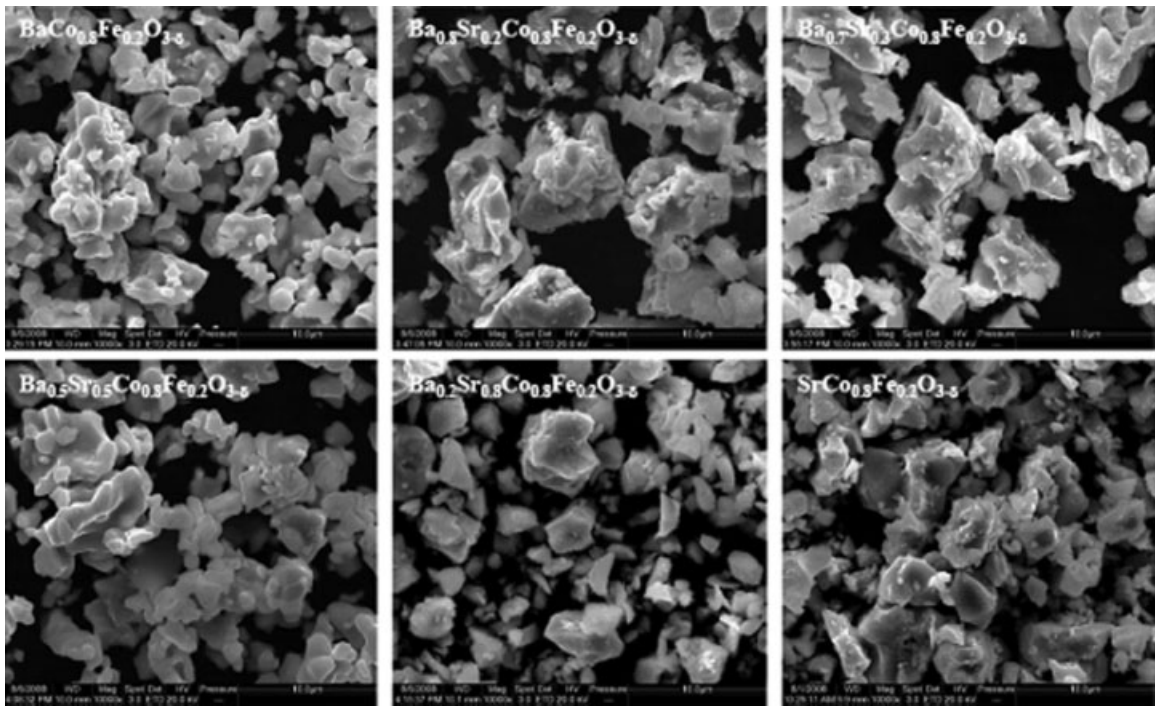

Figure 6. SEM pictures of the as-prepared $Ba_{1-x}Sr_xCo_{0.8}Fe_{0.2}O_{3-\delta}$ oxide powders.

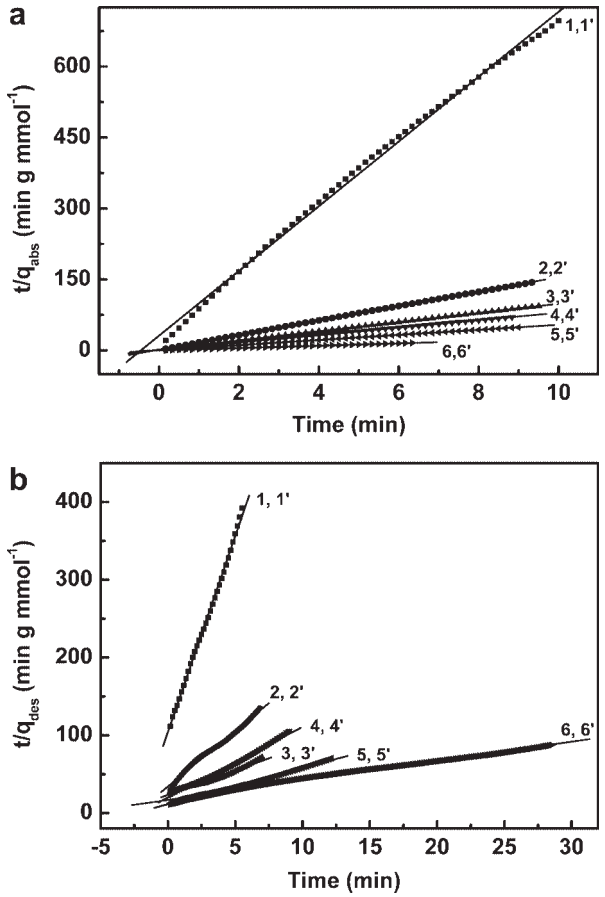

Figure 7. (a) Modeling kinetics lines for the curved sections of the oxygen absorption processes in Figure 4a and (b) modeling kinetics lines for the oxygen desorption processes of Figure 4b.

1,1′. $BaCo_{0.8}Fe_{0.2}O_{3-\delta}$, 2,2′. $Ba_{0.8}Sr_{0.2}Co_{0.8}Fe_{0.2}O_{3-\delta}$, 3,3′. $Ba_{0.7}Sr_{0.3}Co_{0.8}Fe_{0.2}O_{3-\delta}$, 4,4′. $Ba_{0.5}Sr_{0.5}Co_{0.8}Fe_{0.2}O_{3-\delta}$, 5,5′. $Ba_{0.2}Sr_{0.8}Co_{0.8}Fe_{0.2}O_{3-\delta}$, 6,6′. $SrCo_{0.8}Fe_{0.2}O_{3-\delta}$. 1, 2, 3, 4, 5, 6 are the experimental data plots; 1′, 2′, 3′, 4′, 5′, 6′ are the lines determined from kinetics model.

Because the oxides are all synthesized with the same conditions (the wet-chemical EDTA-citric acid complexing method), the aggregated grains are all less than 10 μm, as shown by SEM (Figure 6). Just as for the thin mixed conducting membranes, the oxygen absorption/desorption processes are controlled by the surface oxygen exchange rates and can be simulated by a nonsteady state oxygen transport into or out of those aggregated grains, neglecting oxygen diffusion in the small grains bulk phase. Also, the surface reaction rates are proportional to the different chemical potentials between the surface of the solid grains at time t and that in equilibrium with the atmosphere P_{O2}.[32,33] During an oxygen absorption process, the oxygen absorption capacity q_{abs} is the converse of the oxygen vacancy concentration. Thus, the pseudo-second-order kinetic model equation[34] is used to model the transient rates of oxygen transport into the solid grains for the curved parts of Figure 4a, following the above approach and assuming a uniform oxygen vacancy concentration in the solid grain (as a result of surface reaction rate limiting), as follows:

$$\frac{dq_{abs}}{dt} = k_2\left(q_{eq} - q_t\right)^2 \tag{10}$$

The integrated linear Eq. 11 is known as the Lagergren equation:

$$\frac{t}{q_t} = \frac{1}{k_2 q_{eq}^2} + \frac{1}{q_{eq}} \cdot t \tag{11}$$

where q_{eq} and q_t are the amounts of absorbed oxygen in equilibrium with the surrounding atmosphere at time t, and k_2 is the rate coefficient of the oxygen absorption process. Similar Eqs. 12 and 13 are used for modeling the oxygen desorption kinetics:

$$\frac{dq_{des}}{dt} = k_2'\left(q_{eq}' - q_t\right)^2 \tag{12}$$

$$\frac{t}{q_t} = \frac{1}{k_2' q_{eq}'^2} + \frac{1}{q_{eq}'} \cdot t \tag{13}$$

The plots of the linear equation ((t/q_t) against t) are shown in Figure 7. The slopes and intercepts of these plots are used to calculate the equilibrium absorption (desorption) capacities q_{eq}, (q_{eq}') and the rate coefficient k_2 (k_2'), and the results are shown in Table 1. The data in Table 1 suggest that the fixed-bed oxygen absorption/desorption experimental data fit well the pseudo-second-order kinetics model, although the q_{eq}' (modeling equilibrium oxygen desorption capacity) shows a mismatch with q_{eq} (modeling equilibrium oxygen absorption capacity) at certain times, probably because the oxygen desorption is not complete.

For defect perovskite oxides, the oxygen desorption characteristics are usually studied by the O_2-TPD technique. The desorption of $\alpha(\beta)$ oxygen from an oxide is associated with changes of its B-site ionic valence, and is accommodated by

Table 1. Kinetic Parameters for Modeling the Oxygen Absorption (Desorption) Rates and Data of the Fixed-Bed Oxygen Absorption (Desorption) Capacities at 500°C

Materials	k_2 (k_2') (g mmol^{-1} min^{-1})	q_{eq} (q_{eq}') (mmol/g)	q_{abs} (q_{des}) (mmol/g)	R^2 (R'^2)
$BaCo_{0.8}Fe_{0.2}O_{3-\delta}$	151 (24.3)	0.0146 (0.0199)	0.0143 (0.0140)	0.997 (0.998)
$Ba_{0.8}Sr_{0.2}Co_{0.8}Fe_{0.2}O_{3-\delta}$	126 (5.98)	0.0654 (0.0670)	0.0650 (0.0507)	1.00 (0.992)
$Ba_{0.7}Sr_{0.3}Co_{0.8}Fe_{0.2}O_{3-\delta}$	60.7 (1.67)	0.103 (0.160)	0.101 (0.0978)	1.00 (0.974)
$Ba_{0.5}Sr_{0.5}Co_{0.8}Fe_{0.2}O_{3-\delta}$	83.0 (4.07)	0.127 (0.110)	0.126 (0.0853)	1.00 (0.994)
$Ba_{0.2}Sr_{0.8}Co_{0.8}Fe_{0.2}O_{3-\delta}$	76.5 (1.88)	0.186 (0.215)	0.184 (0.173)	1.00 (0.995)
$SrCo_{0.8}Fe_{0.2}O_{3-\delta}$	113 (0.366)	0.405 (0.402)	0.402 (0.326)	1.00 (0.991)

k_2 (k_2') is the oxygen absorption (desorption) rate coefficient, q_{eq} (q_{eq}') the modeling equilibrium absorption (desorption) capacity, q_{abs} (q_{des}) the fixed-bed oxygen absorption (desorption) capacity and, R^2 (R'^2) the absorption (desorption) correlation coefficient.

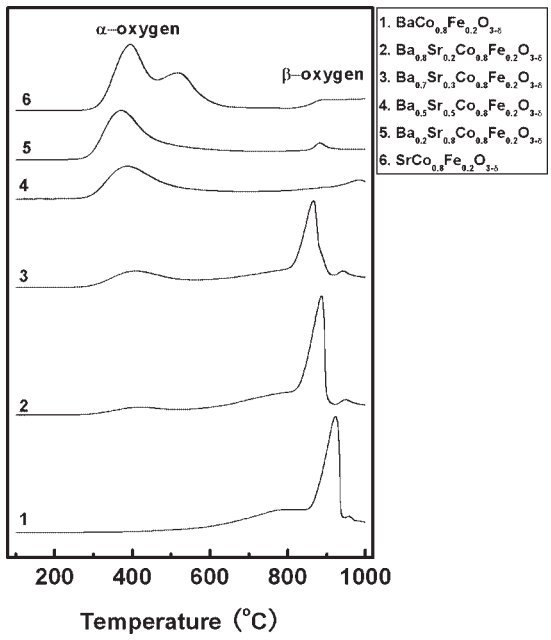

Figure 8. O_2-TPD diagrams of the $Ba_{1-x}Sr_xCo_{0.8}Fe_{0.2}O_{3-\delta}$ oxides.

the oxygen vacancies that occur due to A-site ion substitution. Detailed analysis of the oxygen desorption (or absorption) behavior have already been described.[35,36] As shown in Figure 8, all samples except $BaCo_{0.8}Fe_{0.2}O_{3-\delta}$ exhibit two characteristic desorption peaks, α oxygen and β oxygen, at lower and higher temperature, respectively. Also, the two oxygen desorption peaks relate well to the two oxygen absorption peaks of the fixed-bed oxygen absorption experiments within the two different temperature ranges, as mentioned above (Figure 3). Moreover, another phenomenon appearing in both experiments (O_2-TPD and fixed-bed oxygen absorption) was that, for the series of $Ba_{1-x}Sr_xCo_{0.8}Fe_{0.2}O_{3-\delta}$ oxides, the amounts of oxygen desorbed/absorbed at lower temperatures (300–600°C) increased with Sr content. However, for $SrCo_{0.8}Fe_{0.2}O_{3-\delta}$, two overlapping peaks appeared in the lower temperature range. It is well known that, when trivalent La is substituted by divalent ions, the B-site ions of $La_{1-x}A_xCo_{1-y}Fe_yO_{3-\delta}$ (A = Sr, Ba, Ca) will be oxidized from Co^{3+} (Fe^{3+}) to Co^{4+} (Fe^{4+}), as well as producing oxygen vacancies, and Fe^{3+} is more easily oxidized to Fe^{4+} than Co^{3+}.[20] However, when more Sr^{2+}, with smaller ionic radius, appeared at the A-site, for instance $SrCo_{0.8}Fe_{0.2}O_{3-\delta}$, not only was a lot of Fe^{4+} formed, however, some Co^{4+} ions with smaller ionic radius, appeared, in order to maintain its cubic perovskite structure (tolerance factor $t \approx 1$). Therefore, between the two α oxygen peaks of $SrCo_{0.8}Fe_{0.2}O_{3-\delta}$, the first one may result from the reduction of Co^{4+} to Co^{3+}, and the second from the reduction of Fe^{4+} to Fe^{3+}. For other α desorption peaks of $Ba_{1-x}Sr_xCo_{0.8}Fe_{0.2}O_{3-\delta}$ ($x < 1$), a synergetic effect of the B-site ions (Co^{4+}, Fe^{4+}) gives two smaller α oxygen peaks completely overlapped, because oxides containing Ba^{2+}, which has a bigger ionic radius, gives rise to a larger amount of B^{3+} (or B^{2+}) with bigger B-site ionic radius and less B^{4+}, in order to maintain their perovskite structures. Also, in the O_2-TPD, the higher temperature peaks, excluding the rather weak ones for the single-phase cubic perovskite oxides ($x > 0.3$), become sharp for $Ba_{1-x}Sr_xCo_{0.8}Fe_{0.2}O_{3-\delta}$ ($x = 0$, 0.2, 0.3). The conclusion from the O_2-TPD results is that the introduction of Sr in $BaCo_{0.8}Fe_{0.2}O_{3-\delta}$ facilitates the oxidation of Co^{3+}/Fe^{3+} to Co^{4+}/Fe^{4+} and causes more α-oxygen to be desorbed (or absorbed) in the lower temperature zone. Consequently, $SrCo_{0.8}Fe_{0.2}O_{3-\delta}$ is the best sorbent within the temperature range of 300–600°C, as evidenced by the iodometric titration combined with XRD.

The iodometric titration can be used to determine the average oxidation states of the B-site transition metal ions and the oxygen nonstoichiometry δ of a perovskite-type oxide. Figure 9 shows the average oxidation states of the B-site ions and the largest lower-temperature oxygen absorption capacities of the samples. The average oxidation state of the B-site transition metal ions at room temperature is determined by the iodometric titration, while the largest oxygen absorption capacities in the lower temperature range (300–600°C) are evaluated from Figure 3 ($q_{abs} \sim T$ curves). As shown in Figure 9, although the oxygen absorption capacities of the $Ba_{1-x}Sr_xCo_{0.8}Fe_{0.2}O_{3-\delta}$ oxides decrease with increase of the average radii of the A-site ions, the plot of the average oxidation states of the B-site ions as a function of the average radii of the A-site ions does not exhibit a monotonic curve. For the single-phase cubic perovskite oxides ($Ba_{1-x}Sr_xCo_{0.8}Fe_{0.2}O_{3-\delta}$ with $x > 0.3$), the iodometric titration curve and the oxygen absorption capacity curve have similar trends. That is because, for perovskite-type oxides, the amount of α-oxygen desorbed is determined by the proportion of B-site transition metal ions that are reduced from B^{4+} to B^{3+}. As seen in Figure 2, $BaCo_{0.8}Fe_{0.2}O_{3-\delta}$ and $Ba_{0.8}Sr_{0.2}Co_{0.8}$ $Fe_{0.2}O_{3-\delta}$ are not cubic perovskite oxides, and $Ba_{0.7}Sr_{0.3}Co_{0.8}Fe_{0.2}O_{3-\delta}$ is a transition material between the cubic and noncubic perovskite-type structure oxides, so

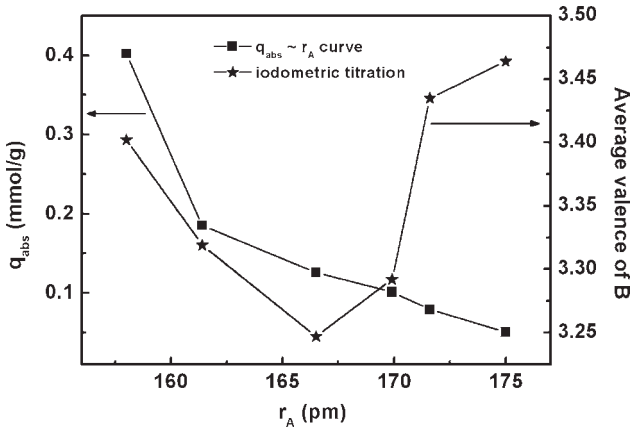

Figure 9. Average oxidation states of the B-site transition metal cations and the largest low-temperature oxygen adsorption capacities versus the average radii of the A-site ions for the $Ba_{1-x}Sr_xCo_{0.8}Fe_{0.2}O_{3-\delta}$ series.

——■—— $q_{abs} \sim r_A$ curve; ——★—— iodometric titration curve.

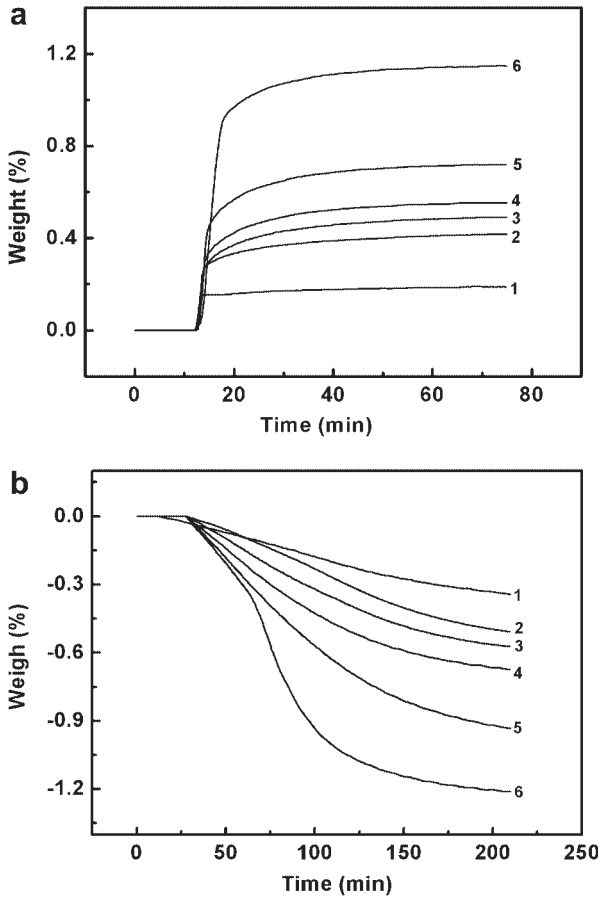

Figure 10. TG curves of the series of $Ba_{1-x}Sr_xCo_{0.8}Fe_{0.2}O_{3-\delta}$: (a) the oxygen absorption processes; (b) the oxygen desorption processes.

1. $BaCo_{0.8}Fe_{0.2}O_{3-\delta}$, 2. $Ba_{0.8}Sr_{0.2}Co_{0.8}Fe_{0.2}O_{3-\delta}$, 3. $Ba_{0.7}Sr_{0.3}Co_{0.8}Fe_{0.2}O_{3-\delta}$, 4. $Ba_{0.5}Sr_{0.5}Co_{0.8}Fe_{0.2}O_{3-\delta}$, 5. $Ba_{0.2}Sr_{0.8}Co_{0.8}Fe_{0.2}O_{3-\delta}$, 6. $SrCo_{0.8}Fe_{0.2}O_{3-\delta}$. $T = 530°C$; Air and N_2 flow rates: 100 ml/min.

they probably have some unusual characteristics that differ from the cubic perovskite-type oxides. This is exemplified by the average oxidation states of the B-site ions as shown in Figure 9, where the transition material $Ba_{0.7}Sr_{0.3}Co_{0.8}Fe_{0.2}O_{3-\delta}$ breaks the step-down trend of the iodometric titration curve. Therefore, $SrCo_{0.8}Fe_{0.2}O_{3-\delta}$, with the highest average oxidation state of the B-site ions and the smallest A-site ion radius among the cubic perovskite oxides of the series $Ba_{1-x}Sr_xCo_{0.8}Fe_{0.2}O_{3-\delta}$ ($x > 0.3$), has the largest oxygen adsorption capacity at low temperature.

The results of the TGA measurements are shown in Figure 10. All the materials studied undergo certain weight changes when they are subjected to switching of the surrounding gases between the synthesized air and high-purity nitrogen. An oxygen desorption process starts when the gas flow is changed from air to nitrogen, while an oxygen absorption process takes place as the gas is switched from nitrogen back to air. All of the oxides have faster oxygen absorption rates than desorption ones, just like the different values of k_2 and k_2' ($k_2 > k_2'$) shown in Table 1, hence the oxygen absorption processes shown in Figure 10a exhibit quite steep breakthrough curves, while the desorption ones in Figure 10b show some "long tails." The most important result from the TGA experiments is that the equilibrium oxygen absorption capacities can be obtained from Figure 10a. It is clear that, at lower temperature (530°C), the equilibrium oxygen absorption capacities of the $Ba_{1-x}Sr_xCo_{0.8}$ $Fe_{0.2}O_{3-\delta}$ series increase as the average radii of the A-site ions are reduced, and the tend is consistent with the results of the O_2-TPD and fixed-bed oxygen absorption experiments in the temperature range of 300–600°C. Thus $SrCo_{0.8}Fe_{0.2}O_{3-\delta}$ has the largest oxygen absorption (desorption) capacity in the low temperature range investigated.

Conclusions

In this article, the oxygen absorption properties of the series of $Ba_{1-x}Sr_xCo_{0.8}Fe_{0.2}O_{3-\delta}$ oxides have been systemically examined by oxygen partial pressure swing absorption at temperature $T \geq 300°C$. As expected, all the perovskite oxides exhibited some oxygen absorption capacities in the temperature range of 300–600°C, which increased as the average radii of the A-site ions decreased. Hence, the material $SrCo_{0.8}Fe_{0.2}O_{3-\delta}$, with the smallest A-site ionic radius, had the largest oxygen absorption capacity at lower temperature (500°C). In contrast, $BaCo_{0.8}Fe_{0.2}O_{3-\delta}$ absorbed the largest amount of oxygen ($q_{abs} = 0.533$ mmol/g) at higher temperature (850°C). The pseudo-second-order kinetics model is a good model for the fixed-bed oxygen absorption experiment. The X-ray diffraction results showed that the series $Ba_{1-x}Sr_xCo_{0.8}Fe_{0.2}O_{3-\delta}$ with $x > 0.3$ had a single-phase cubic perovskite structure. The oxygen absorption (desorption) properties of this series were also investigated by TPD, iodometric titration, and TG techniques, which have further confirmed the fixed-bed oxygen absorption properties of all the studied materials.

When compared with conventional PSA absorbents (zeolites) used for air separation, this new type of oxygen absorbents, perovskite-type oxides with an oxygen deficient structure, exhibits many merits, such as large oxygen absorption capacities and an infinite selectivity for oxygen. Taking these advantages into account, the perovskite-type oxides will be a good candidate for oxygen separation from air or other oxygen-containing gases. Furthermore, if the oxygen partial pressure swing absorption technique is combined with the oxygen permeation processes of dense membranes, two high-purity and very important industrial products, O_2 and N_2, will be obtained.[37]

Acknowledgments

This work was supported by the National Science Fund for Distinguished Young Scholars (20725313), and the Ministry of Science and Technology of China (Grant No. 2005CB221404).

Notation

F_{air} = flux of the synthesized air (ml min^{-1})
F_{He} = flux of the pure helium (ml min^{-1})
F_{out} = flux of the effluent exiting from the absorption column (ml min^{-1})
k_o = rate coefficient for the line parts of the Figure 4a (ml min^{-1} g^{-1})
k_2 = pseudo-second-order rate coefficient for the curved parts of Figure 4a (g $mmol^{-1}$ min^{-1})
k_2' = pseudo-second-order rate coefficient for oxygen desorption processes (g $mmol^{-1}$ min^{-1})

m = weight of an oxide absorbent (g)
q_{abs} = oxygen absorption capacity (mmol g^{-1})
$q_{abs(1)}$ = oxygen absorption capacity for the low plane parts in Figure 5 (mmol g^{-1})
q_{des} = oxygen desorption capacity (mmol g^{-1})
q_{eq} = modeling equilibrium absorption capacity (mmol g^{-1})
q_{eq}' = modeling equilibrium desorption capacity (mmol g^{-1})
q_t = oxygen absorption/desorption capacity at time t (mmol g^{-1})
r_A = average radius of A-site cations of an oxide (pm)
R^2 = absorption correlation coefficient
R'^2 = desorption correlation coefficient
t = oxygen absorption/desorption time (min)
x_{in} = oxygen mole fraction in the feed air
x_{O2} = oxygen mole fraction in the effluent exiting from the absorption column
x_{out} = oxygen mole fraction in the F_{out}

Literature Cited

1. Zhang Y, Wang Z, Ji SL. *Oxygen-Enriched Technologies and Their Applications*. Beijing: Chemical Industry Press, 2005:7–9.
2. Jayaraman A, Yang RT. Stable oxygen-selective sorbents for air separation. *Chem Eng Sci*. 2005;60:625–634.
3. Lin YS, MacLean DL, Zeng YX. *High-Temperature Adsorption Process*. US Patent 6,059,858, 2000.
4. Yang ZH, Lin YS, Zeng Y. High-temperature sorption process for air separation and oxygen removal. *Ind Eng Chem Res*. 2002;41: 2775–2784.
5. Karppinen M, Yamauchi H, Otani S, Fujita T, Motohashi T, Huang YH, Valkeapaa M, Fjellvag H. Oxygen nonstoichiometry in $YBaCo_4O_{7+\delta}$: large low-temperature oxygen absorption/desorption capability. *Chem Mater*. 2006;18:490–494.
6. Hao HS, Cui JH, Chen CQ, Pan LJ, Hu J, Hu X. Oxygen adsorption properties of $YBaCo_4O_7$-type compounds. *Solid State Ionics*. 2006; 177:631–637.
7. Hu J, Hu X, Hao H, Guo L, Song H, Yang D. A transient thermogravimetric study on the oxygen permeation at high temperature of the superconducting material $YBa_2Cu_3O_{7-\delta}$. *Solid State Ionics*. 2005; 176:487–494.
8. Yang D, Lu H, Song H, Mo J, Li G, Chen C, Guo Y, Hu X. Experimental study of oxygen diffusion and permeation through $YBa_2Cu_3O_{7-x}$ membranes. *J Membr Sci*. 2004;233:45–50.
9. Hao HS, Zheng L, Wang YF, Liu SJ, Hu X. Thermogravimetric study on oxygen adsorption/desorption properties of double perovskite structure oxides $REBaCo_2O_{5+\delta}$ (RE = Pr, Gd, Y). *J Rare Earths*. 2007;25:275–281.
10. Guntuka S, Banerjee S, Farooq S, Srinivasan MP. A- and B-site substituted lanthanum cobaltite perovskite as high temperature oxygen sorbent. 1. Thermogravimetric analysis of equilibrium and kinetics. *Ind Eng Chem Res*. 2008;47:154–162.
11. Guntuka S, Farooq S, Rajendran A. A- and B-Site substituted lanthanum cobaltite perovskite as high temperature oxygen sorbent. 2. Column dynamics study. *Ind Eng Chem Res*. 2008;47:163–170.
12. Tsai CY, Dixon AG, Ma YH, Moser WR, Pascucci MR. Dense perovskite, $La_{1-x}A'_xFe_{1-y}Co_yO_{3-\delta}$ (A' = Ba, Sr, Ca), membrane synthesis, applications, and characterization. *J Am Ceram Soc*. 1998;81: 1437–1444.
13. Yamazoe N, Teraoka Y, Seiyama T. TPD and XPS study on thermal behavior of absorbed oxygen in $La_{1-x}Sr_xCoO_{3-\delta}$. *Chem Lett*. 1981; 1767–1770.
14. Yamazoe N, Furukawa S, Teraoka Y, Seiyama T. The effect of oxygen sorption on the crystal structure of $La_{1-x}Sr_xCoO_{3-\delta}$. *Chem Lett*. 1982;2019–2022.
15. Teraoka Y, Zhang HM, Yamazoe N. Oxygen-sorption properties of defect perovskite-type $La_{1-x}Sr_xCo_{1-y}Fe_yO_{3-\delta}$. *Chem Lett*. 1985;1367–1370.
16. Wang HH, Wang R, Liang DT, Yang WS. Experimental and modeling studies on $Ba_{05}Sr_{05}Co_{08}Fe_{02}O_{3-\delta}$ (BSCF) tubular membranes for air separation. *J Membr Sci*. 2004;243:405–415.
17. Bouwmeester HJM. Dense ceramic membranes for methane conversion. *Catal Today*. 2003;82:141–150.
18. Ezin AN, Kurumchin EK, Murygin IV, Tsidilkovski VI, Vdovin GK. The types of surface exchange and diffusion of oxygen in $La_{0.7}Sr_{0.3}CoO_{3-\delta}$. *Solid State Ionics*. 1998;112:117–122.
19. Qiu L, Lee TH, Liu LM, Yang YL, Jacobson AJ. Oxygen permeation studies of $SrCo_{0.8}Fe_{0.2}O_{3-\delta}$. *Solid State Ionics*. 1995;76:321–329.
20. Stevenson JW, Armstrong TR, Carneim RD, Pederson LR, Weber WJ. Electrochemical properties of mixed conducting perovskites $La_{1-x}M_xCo_{1-y}Fe_yO_{3-\delta}$ (M = Sr, Ba, Ca). *J Electrochem Soc*. 1996; 143:2722–2729.
21. Sunarso J, Baumann S, Serra JM, Meulenberg WA, Liu S, Lin YS, Diniz da Costa JC. Mixed ionic-electronic conducting (MIEC) ceramic-based membranes for oxygen separation. *J Membr Sci*. 2008; 320:13–41.
22. Kharton VV, Kovalevsk AV, Patrakeev MV, Tsipis EV, Viskup AP, Kolotygin VA, Yaremchenko AA, Shaula AL, Kiselev EA, Waerenborgh JC. Oxygen nonstoichiometry, mixed conductivity, and mossbauer spectra of Ln(0.5)A(0.5)FeO(3-delta) (Ln = La-Sm, A = Sr, Ba): effects of cation size. *Chem Mater*. 2008;20:6457–6467.
23. Li SG, Jin WQ, Huang P, Xu NP, Shi J, Lin YS, Hu MZC, Payzant EA. Comparison of oxygen permeability and stability of perovskite type $La_{0.2}A_{0.8}Co_{0.2}Fe_{0.8}O_{3-\delta}$ (A = Sr, Ba, Ca) membranes. *Ind Eng Chem Res*. 1999;38:2963–2972.
24. Shao, ZP, Xiong GX, Tong JH, Dong H, Yang WS. Ba effect in doped $Sr(Co_{08}Fe_{02})O_{3-\delta}$ on the phase structure and oxygen permeation properties of the dense ceramic membranes. *Sep Purif Technol*. 2001;25:419–429.
25. Dyer PN, Richards RE, Russek SL, Taylor DM. Ion transport membrane technology for oxygen separation and syngas production. *Solid State Ionics*. 2000;134:21–33.
26. Lin YS. Microporous and dense inorganic membranes: current status and prospective. *Sep Purif Technol*. 2001;25:39–55.
27. Shao ZP, Yang WS, Cong Y, Dong H, Tong JH, Xiong GX. Investigation of the permeation behavior and stability of a $Ba_{0.5}Sr_{0.5}Co_{0.8}Fe_{0.2}O_{3-\delta}$ oxygen membrane. *J Membr Sci*. 2000;172:177–188.
28. Karppinen M, Matvejeff M, Salomaki K, Yamauchi H. Oxygen content analysis of functional perovskite-derived cobalt oxides. *J Mater Chem*. 2002;12:1761–1764.
29. Karppinen M, Fukuoka A, Niinisto L, Yamauchi H. Determination of oxygen content and metal valences in oxide superconductors by chemical methods. *Supercond Sci Technol*. 1996;9:121–135.
30. Zhu XF, Wang HH, Yang WS. Structural stability and oxygen permeability of cerium lightly doped $BaFeO_{3-\delta}$ ceramic membranes. *Solid State Ionics*. 2006;177:2917–2921.
31. Malek A, Farooq S, Rathor MN, Hidajat K. Effect of velocity variation due to adsorption-desorption on equilibrium data from breakthrough experiments. *Chem Eng Sci*. 1995;50:737–740.
32. van Hassel BA, Kawada T, Sakai N, Yokokawa H, Dokiya M, Bouwmeester HJM. Oxygen permeation modelling of perovskites. *Solid State Ionics*. 1993;66:295–305.
33. Zeng Y, Lin YS. A transient TGA study on oxygen permeation properties of perovskite-type ceramic membrane. *Solid State Ionics*. 1998;110:209–221.
34. Marczewski AW. Kinetics and equilibrium of adsorption of organic solutes on mesoporous carbons. *Appl Surf Sci*. 2007;253:5818–5826.
35. Teraoka Y, Yoshimatsu M, Yamazoe N, Seiyama T. Oxygen-sorptive properties and defect structure of perovskite-type oxides. *Chem Lett*. 1984;893–896.
36. Yamazoe N, Teraoka Y. Oxidation catalysis of perovskites-relationships to bulk structure and composition (valency, defect, etc.). *Catal Today*. 1990;8:175–199.
37. Zhu XF, Sun SM, He YF, Cong Y, Yang WS. New concept on air separation. *J Membr Sci*. 2008;323:221–224.

Manuscript received Jan. 20, 2009, and revision received Mar. 27, 2009.